On the strength-ductility modifications in pure copper after severe plastic deformation

Pouya Tajdary [a], Léo Morin [b,*], Chedly Braham [a], Omar Novelo Peralta [c], Gonzalo Gonzalez [c]

[a] PIMM, Arts et Metiers Institute of Technology, CNRS UMR 8006, Cnam, HESAM University, 151 boulevard de l'Hopital, 75013 Paris, France
[b] Univ. Bordeaux, Arts et Metiers Institute of Technology, CNRS, Bordeaux INP, I2M, UMR 5295, F-33400, Talence, France
[c] Instituto de Investigaciones en Materiales, Universidad Nacional Autónoma de México, Circuito Exterior S/N, Cd. Universitaria, A.P. 70-360, Coyoacán, 04360, México, D.F., Mexico

Keywords:
Strength-ductility trade-off
Gurson's model
Dislocation-based hardening
Severe plastic deformation

A B S T R A C T

The aim of this work is to investigate experimentally and numerically the modifications of both strength and ductility after processing by severe plastic deformation, using several passes of repetitive corrugation and straightening on sheets made of pure copper. Experimental stress–strain curves are determined before and after processing in order to study the influence of the process on the mechanical properties. The modeling of the mechanisms responsible of the mechanical properties evolution is done through the development of an extended Gurson model including a dislocation-based modeling of hardening. The model developed is implemented into a finite element code and applied to the numerical prediction of the repetitive corrugation and straightening followed by a tensile test. The modifications of strength and ductility predicted numerically are qualitatively in good agreement with the experimental observations.

1. Introduction

Strength and ductility of a material are fundamental properties in structural applications which are typically opposed. Strength generally refers to the ability of a material to withstand a load without plastic deformation or failure: it can thus be characterized either by the yield stress or the ultimate stress (and more generally by the whole hardening curve). On the other hand, ductility generally refers to the ability of a material to deform in tension before failure (Gensamer, 2017). These two properties can notably be characterized by a tensile test.

The strength of a metallic material is related to several factors at the micro-scale including the grain size, the increase of the dislocation densities, dislocation patterning and the presence of precipitates, among others (Estrin, 1998). During mechanical loading, the evolution of these parameters leads to strain hardening which increases the strength. Ductility, on the other hand, is influenced by several factors such as crystal structure, grain size, as well as the change in dislocation density as a function of strain, and is mostly tied to the strain at macroscopic localization which is driven by a combination of macroscopic shear band and microscopic void coalescence (Tekoglu et al., 2015). This onset of flow localization results from several factors including the loading mode and the initial microstructure (second-phase particles, initial micro-voids etc.). Processing by plastic deformation will thus result in a deep modification of the mechanical properties of a material. Indeed, plastic deformation increases the strength due to hardening but it decreases ductility by accelerating the occurrence of ductile damage: this is the so-called strength-ductility trade-off (Ritchie, 2011).

Several attempts have been proposed to evade the strength-ductility tradeoff, by combining high strength and ductility, with the rise of nanocrystalline materials, by means of gradient hierarchical nanotwins (Wei et al., 2014), gradient nanograined structures (Lu, 2014) and lamella structures (Wu et al., 2015), among others. Mention has to be made to severe plastic deformation (SPD) processing which refers to a class of metalworking processes that allows to produce high-strength materials without sacrificing much the ductility (Valiev et al., 2016). During SPD processes, the material is subjected to significant plastic deformation without much change in its initial geometry, leading to the formation of ultrafine-grained structures with high-angle and non-equilibrium grain boundaries capable of grain-boundary sliding which can greatly contribute to an important ductility (Valiev, 2004). The most common SPD processes are equal channel angular pressing (ECAP) (Kawasaki et al., 2009), high torsion pressing (HTP) (Bhovi et al., 2016), accumulative roll bonding (ARB) (Inoue and Tsuji, 2009) and repetitive corrugation and straightening (RCS) (Huang et al., 2001).

The present work is concerned with the process RCS which is considered as a promising metal forming process of large-scale sheet

* Corresponding author.
E-mail address: leo.morin@u-bordeaux.fr (L. Morin).

https://doi.org/10.1016/j.mechmat.2024.105028

metals with nanostructures (Huang et al., 2001). The principle of the process is to (i) deform a sheet using a multi-pattern corrugation die (corrugation step) and (ii) a straightening die deforms the material to its initial shape (straightening step). As the workpiece is flat at the end of straightening step, the process can be repeated in order to induce important deformation which may lead to grain refinement. RCS is suitable for metal sheets, and different dies that optimize shear deformation have been tested in the literature (Thangapandian et al., 2016). The proposed die workpiece referred in this work has been reviewed and discussed in previous works (Elizalde et al., 2020; Reyes-Ruiz et al., 2021), applied to different aluminium alloys. In general terms, independent of which alloy is processed by RCS, mechanical strength increases, grain size decreases, the original texture disappears, and a new texture is generated (Alvarado et al., 2020). From a numerical point of view, the deformation gradient has been calculated for this die workpiece (Ezequiel et al., 2020b; Elizalde et al., 2020), and the formability effect due to the RCS process has been reported (Ezequiel et al., 2020a; Elizalde et al., 2021), noting that more than 2 RCS passes are useless for the mechanical properties. The modification of the microstructure induced by RCS is associated with an increase of the yield and ultimate strengths. In the work of Elizalde et al. (2020), tensile tests have been performed after several passes of the process in aluminum alloys Al-6061: the yield strength is increasing with the passes while ductility decreases. Similar observations were made in several alloys including pure aluminum (Shirdel et al., 2010; Rahimi et al., 2018), aluminum alloys (Hajizadeh et al., 2017; Bhovi et al., 2018; Elizalde et al., 2020; Ezequiel et al., 2020b; Morin et al., 2021), copper (Torkestani and Dashtbayazi, 2018) and magnesium alloys (Nor et al., 2020).

From the modeling point of view, the description of the strength-ductility trade-off (and its possible evading) requires to consider the effect of plastic deformation simultaneously on both hardening and ductile damage. Nonetheless, physically-based and micromechanical models aiming at describing strain hardening or ductile damage evolution have followed separated paths:

- Physically-based models of strengthening have been mainly developed in the physical metallurgy community under the form of microstructure-related constitutive models based on the dislocation theory (Estrin, 1998). They have been proposed as alternatives to standard macroscopic approaches (based on power-law hardening laws and calibrated from macroscopic tensile tests) by accounting for the description of dislocation cell structures (with possible grain refinement). Plastic flow is then described by several mechanisms including dislocation storage and concurrent dislocation annihilation by recovery as well as dynamic recovery mechanisms. The most advanced modeling framework is based on the pioneering works of Mughrabi (1983) and Estrin et al. (1998), based on the description of dislocation densities in cell walls and cell interiors. The shrinkage of cell walls is accounted for in this approach and this permits to describe the effect of grain refinement on strengthening. The advantages of these physically-based approaches over macroscopic hardening laws are that it can (i) account for all hardening stages (including stages III and IV) and (ii) they contain a relatively small number of adjustable material parameters with a clear physical meaning. Therefore, the effect of metallurgical variables (such as, e.g., solute concentration, grain size, spacing between second phase particle) on the macroscopic mechanical behavior can be predicted.
- Micromechanical models of ductile failure are based on the pioneering work of Gurson (1977) who performed a limit-analysis of a spherical cell containing a spherical void (representing a representative cell of a porous material). This model, initially developed to reproduce void growth (and restricted to perfect plasticity), has then been extended by Tvergaard and Needleman (1984) to include void nucleation and coalescence allowing the simulation of the three main mechanisms involved in ductile failure: this is the so-called GTN model. Due to the intrinsic limitations of the GTN model (isotropic materials, spherical voids, etc.), numerous extensions have been derived to account for anisotropic materials, shear-dominated loadings, size effects, among others (Benzerga et al., 2016). It must be noted that Gurson-type models are by essence restricted to rigid-plastic materials since they are based on limit-analysis (Leblond et al., 2018); however hardening can be easily accounted for by replacing the yield stress in the macroscopic criterion by some average yield stress (in an equivalent fictitious homogeneous material), whose evolution equation is provided by an approximate equality of the plastic dissipations in the heterogeneous porous material and the equivalent material. Mention has to be made to the work of Morin et al. (2017b) (in the context of cyclic ductile failure) which extends Gurson's model to hardening effects directly in the limit-analysis procedure using sequential limit-analysis which allows to consider hardening effects as a pre-hardening which modifies plastic flow (Leblond et al., 2018).

It is important to note that Gurson-type models are generally used together with macroscopic power-law hardening models (and not physically-based models of hardening) because this class of models is mainly used to simulate experimental tests of failure of ductile materials. In addition, physically-based models of hardening have been developed in the context of the simulation of severe plastic deformation processes, which are designed so as to avoid the occurrence of damage which can explain that their use in the context of ductile failure is scarce. Mention has to be made to the works of Jafari et al. (2014) and Chen et al. (2019), in which a single-parameter Estrin-type model was considered in some GTN-like model. The effect of dislocation can therefore be accounted for in these approaches but it cannot provide an estimate of the grain size making these models not suitable for severe plastic deformation processes.

The aim of this work is to investigate experimentally and numerically the evolution of strength and ductility after processing by severe plastic deformation (SPD). We will consider a model problem of pure copper subjected to repetitive corrugation and straightening (RCS) which is an interesting metal forming process for production of large-scale nanostructured sheet metals (Huang et al., 2001). Tensile tests are performed before and after the process in order to study the evolution of strength and ductility after processing. In order to simulate numerically this evolution, we will develop a model of metal plasticity accounting for the local mechanisms responsible for the strength and ductility and their possible evolution during plastic straining. This model will be based on a coupling between a micromechanical Gurson-type model (to model ductile damage) and a suitable modification of a physically-based Estrin-type model (to model hardening at large strains).

The rest of the paper is organized as follows. In Section 2, the experimental procedures of repetitive corrugation and straightening on pure copper are presented. An extended Gurson-type model accounting for dislocation density based plasticity is developed in Section 3. The model developed is then implemented numerically and we study the maximum grain refinement achievable before coalescence in Section 4. Finally in Section 5, we perform, using the model developed, finite element simulations of the RCS process followed by a tensile in order to study numerically the evolution of strength and ductility after processing.

2. Experimental procedures

2.1. Material

The material considered is a 99.9% pure copper. It was chosen because (i) it has a high ductility and (ii) it has been widely used in

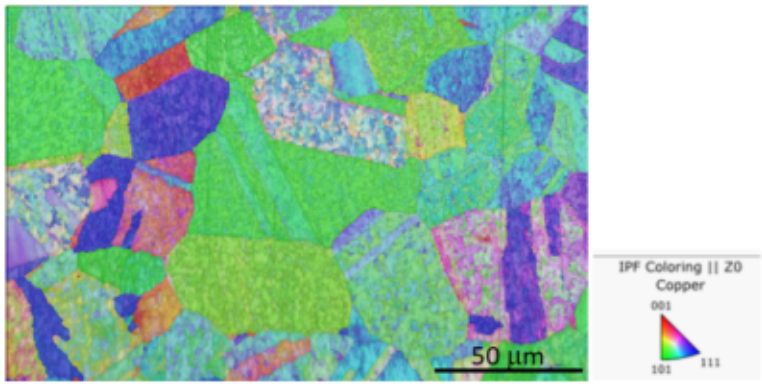

Fig. 1. Characteristic microstructure of Cu samples prior to RCS process. (For interpretation of the references to color in this figure legend, the reader is referred to the web version of this article.)

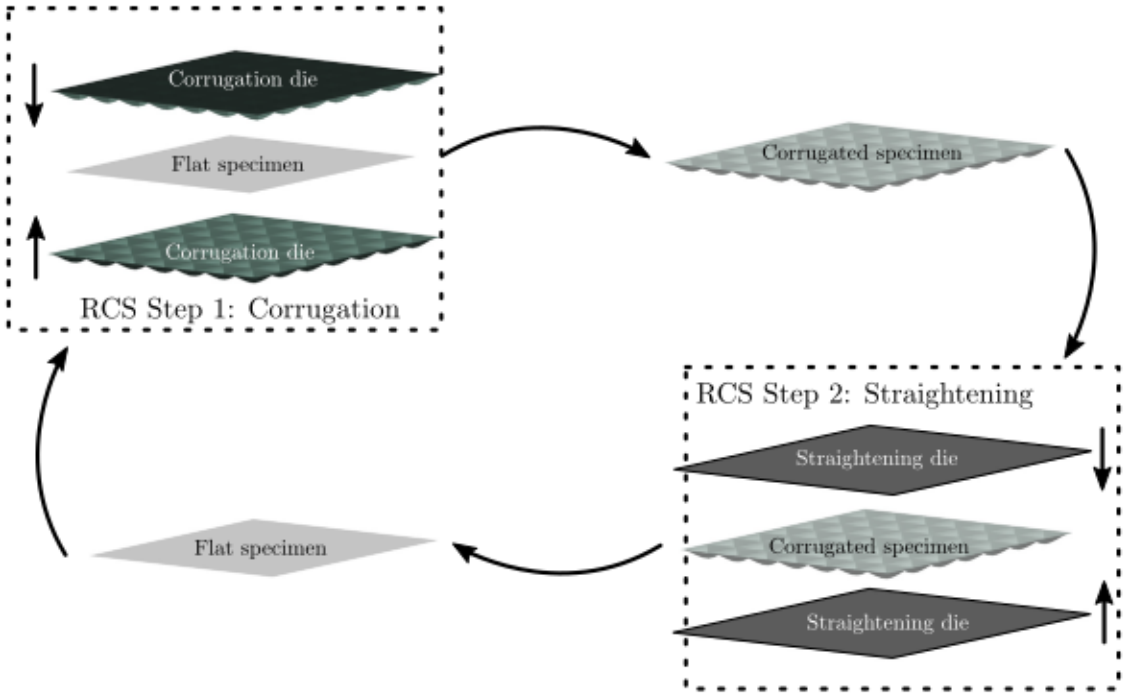

Fig. 2. Description of processing by repetitive corrugation and straightening.

several SPD processes (Toth et al., 2001; Zenasni et al., 2019) which makes it a good candidate to investigate modifications in strength and ductility. A 610 × 300 mm cold rolled plate of 0.8 mm thickness was initially cut to a 125 × 125 mm size. An annealing heat treatment is applied to enhance the ductility and remove residual stress as well as grain distortions due to the previous rolling process. The samples were kept at 550 °C temperature for three hours before cooling to room temperature.

In addition, the copper initial microstructure, before RCS process, was analyzed by the EBSD technique, (carried out with SEM JEOL 7600 equipped with a QUANTAX CRYSTALIGN 200 detector), and shown in Fig. 1; it reveals equiaxial grains with an equivalent diameter of about 50 µm, as well as some grains twinned, well identified by their characteristic parallel bands. On the other hand, a preferred orientation was visible by the inverse pole figure IPFZ, in which most grains are greenish, i.e, near to (101).

2.2. Processing by repetitive corrugation and straightening (RCS)

Repetitive corrugation and straightening (RCS) is a process based on the forming of workpiece using multi-pattern corrugation dies followed by a straightening using flat dies (see Fig. 2):

(1) An initial flat sheet is corrugated using two corrugation dies, which induces important shear deformation within the sheet. At the end of this step, the specimen is no longer a sheet as its shape is corrugated.
(2) The corrugated specimen is then straightened using two flat straightening dies. At the end of this step, the specimen is again a flat sheet.

These two steps correspond to one *pass*. Since at the end of a pass the specimen is flat, it is possible to repeat these passes in order to increase the shear deformation, which ultimately leads to some grain refinement (Huang et al., 2004).

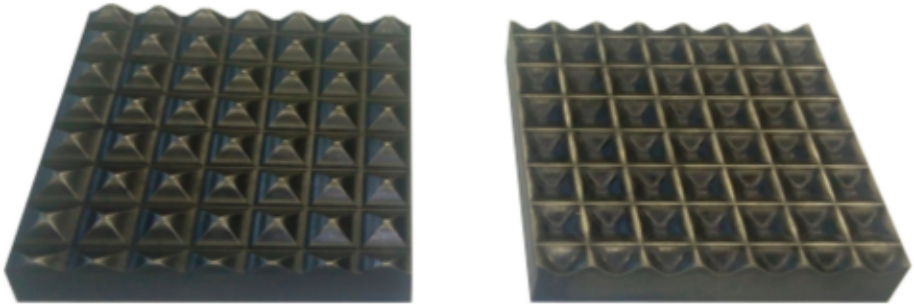

Fig. 3. Description of the corrugation die.

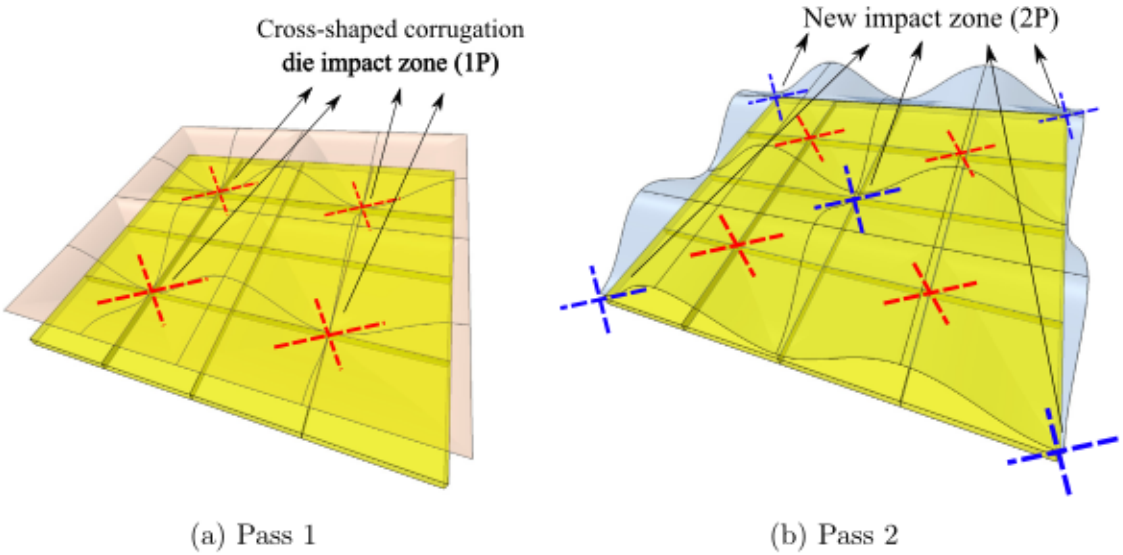

Fig. 4. Shifting of the corrugation die patterns along the sheet metal specimen after 1st pass. (a) The part of sheet metal shown in the image will undergo corrugation in pass 1 and two patterns will be formed. (b) The corrugation die turned upside-down and is shifted half a pattern and in pass 2, the previous two patterns will now become one pattern in the middle with two half patterns on both sides.

We consider the experimental set-up developed by Ezequiel et al. (2020b): the corrugation die profile is based on two perpendicular sinusoidal functions of period 16 mm and is composed of 7×7 elementary patterns (see Fig. 3). For the first pass, corrugation and straightening dies are used on the initial sheet metal sample. For the second pass, the specimen is turned upside-down and moved by a distance of half the corrugation period (8 mm) in the $x-$direction, as shown in Fig. 4. This permits to increase the homogeneity of the mechanical fields (which are very heterogeneous after the first pass).

The process was performed at a speed of 2 mm/min using an Instron 8802 servo-hydraulic machine with 250 kN maximum load capacity. Additionally, a very thin layer of Teflon has been placed between the sheet metal and the dies in order to reduce the friction. A representation of the workpiece after two passes of the process is provided in Fig. 5

2.3. Tensile test

Before the RCS process and after pass 2, tensile tests are performed in order to investigate the effect of the process on the strength-ductility trade-off. The tensile specimen were cut according to ASTM E8M standard with a gauge dimension of 37×7 mm (see Fig. 6).

The tensile tests were performed at deformation speed of 0.5 mm/min (which is equivalent to about 10^{-5} m/s) using an Instron 1125 universal testing machine with 100 kN loading capacity. Very slow deformation rates are used to perform quasi-static experiments and avoid strain rate effects. A G51-12MA Instron extensometer was also used to measure the strain.

Fig. 5. Workpiece after two passes of the RCS.

3. A Gurson-type model accounting for dislocation density based plasticity

In this section, an extended Gurson model including dislocation density evolution is developed. Conventional hardening laws, such as Voce or Swift are not suitable for severe plastic deformations when the material undergoes very high strains with important changes in

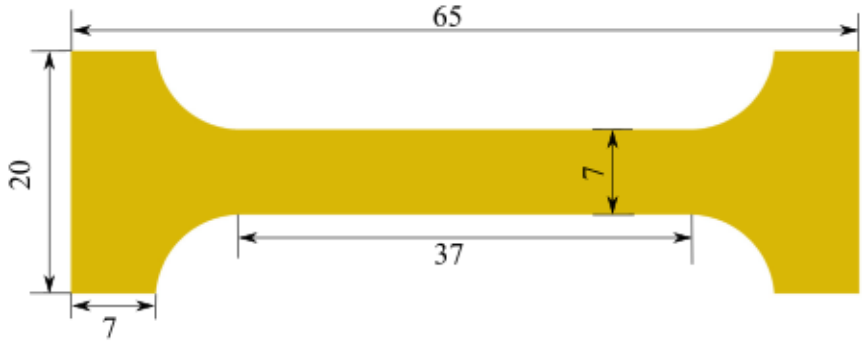

Fig. 6. Dimension of the tensile test specimen.

the microstructure. Hence, in order to include the effect of both hardening, grain refinement, and ductile damage, an extension of Gurson (1977)'s micromechanical damage model is proposed based on the evolution of dislocation cell structures in the matrix surrounding the void. A physically-based model of hardening will be adapted from the composite model developed by Estrin et al. (1998).

3.1. GTN model

We first recall the main ingredients of the standard GTN model (Tvergaard and Needleman, 1984). This model is based on Gurson (1977)'s criterion which has been obtained from the limit-analysis of a spherical cell containing a spherical void and subjected to conditions of homogeneous boundary strain rate. This model is thus suitable for ductile fracture at moderate to high stress triaxiality (for which void shape effects are moderate).

The macroscopic yield criterion reads

$$\Phi(\boldsymbol{\sigma}, \bar{\sigma}, f) = \frac{\sigma_{eq}^2}{\bar{\sigma}^2} + 2qf\cosh\left(\frac{3\sigma_m}{2\bar{\sigma}}\right) - 1 - (qf)^2 \leq 0, \tag{1}$$

where σ_{eq} is the macroscopic equivalent von Mises stress, σ_m is the macroscopic mean stress, $\bar{\sigma}$ is the yield stress of the matrix, f is the porosity (corresponding to the volume fraction of voids) and q is Tvergaard's parameter.

The macroscopic flow rule, deduced from the normality property reads

$$\boldsymbol{D}^p = \dot{\lambda}\frac{\partial \Phi}{\partial \boldsymbol{\sigma}}(\boldsymbol{\sigma}, \bar{\sigma}, f) \quad , \quad \dot{\lambda}\begin{cases} = 0 & \text{if} \quad \Phi(\boldsymbol{\sigma}, f, \bar{\sigma}) < 0 \\ \geq 0 & \text{if} \quad \Phi(\boldsymbol{\sigma}, f, \bar{\sigma}) = 0, \end{cases} \tag{2}$$

where $\boldsymbol{D}^p$ is the Eulerian plastic strain rate and $\dot{\lambda}$ is the plastic multiplier.

Following Gurson's approach, hardening is considered by assuming that the plastic dissipation in the RVE is equal to the plastic dissipation in some fictitious "equivalent material" with the same volume fraction of porosity f:

$$\boldsymbol{\sigma} : \boldsymbol{D}^p = (1-f)\bar{\sigma}\dot{\bar{\varepsilon}}. \tag{3}$$

In this equation, the yield stress $\bar{\sigma}$ is a non-linear function of the equivalent strain $\bar{\varepsilon}$, which will be described by a dislocation density based model.

The evolution equation of the porosity (due to void growth) is classically deduced from the matrix incompressibility:

$$\dot{f}_{\text{growth}} = (1-f)\,\text{tr}\,\mathbf{D}^p. \tag{4}$$

Void nucleation is described by the strain-controlled term of Chu and Needleman (1980)'s heuristic model. The total nucleation rate is given by

$$\dot{f}_{\text{nucleation}} = \frac{f_N}{s_N\sqrt{2\pi}}\exp\left[-\frac{1}{2}\left(\frac{\bar{\varepsilon}-\varepsilon_N}{s_N}\right)^2\right]\times\dot{\bar{\varepsilon}}, \tag{5}$$

where f_N, ε_N and s_N respectively represent the volume fraction, average nucleation strain and standard deviation of the nucleating voids. The evolution equation of the porosity thus reads

$$\dot{f} = \dot{f}_{\text{growth}} + \dot{f}_{\text{nucleation}}. \tag{6}$$

Finally void coalescence is classically accounted for by using Tvergaard and Needleman (1984)'s classical modification of Gurson (1977)'s model, which consists in replacing the porosity f by some larger fictitious one f^*, once some "critical value" f_c has been reached:

$$f^* = \begin{cases} f & \text{if} \quad f \leq f_c \\ f_c + \delta(f - f_c) & \text{if} \quad f > f_c, \end{cases} \tag{7}$$

where f_c and $\delta > 1$ are material parameters.

3.2. Dislocation-based model of hardening

In order to account for severe plastic deformation (and their consequences upon grain refinement), a dislocation-based model of hardening, based on the pioneering work of Estrin et al. (1998), is considered. The advantage of this modeling is that it can account for all hardening stages (and especially stage III and IV). This approach is based on a description of the dislocation substructures as a composite model, made of cell interiors and walls, in which the dislocation densities have different evolution equations. The model of Estrin et al. (1998), initially developed in a 2D case, has been extended to 3D loadings by Toth et al. (2001), through some appropriate modifications of the dislocation density evolution laws.

It is important to note that, in this approach, strain rate effects permit the description of dynamic recovery process by dislocation cross-slip. Nonetheless, since Gurson's model has been developed using limit-analysis theory, it is restricted by essence to rate-independent materials (Leblond et al., 2018). As a consequence, we will consider a rate-independent version of Estrin et al. (1998)'s model in order to make this model compatible with Gurson's framework.

A "composite microstructure", made of cells and walls is considered to describe the microstructure. In this model, the equivalent resolved shear stress τ depends on the resolved shear stress in each phase (denoted by τ_w in the walls and τ_i in the cell interior) using a rule of mixture:

$$\tau = v_w\tau_w + v_i\tau_i, \tag{8}$$

where v_w and $v_i = 1 - v_w$ are respectively the volume fraction of walls and cell interiors. Using the Taylor factor M, the yield stress $\bar{\sigma}$ used in Gurson's model can be express in terms of the equivalent critical resolved shear stress τ:

$$\bar{\sigma} = \frac{\tau}{M}. \tag{9}$$

In the limit of quasi-static loadings, the resolved shear stresses in each phase are given by

$$\begin{cases} \tau_w &= \alpha\mu b\sqrt{\rho_w} \\ \tau_i &= \alpha\mu b\sqrt{\rho_i}, \end{cases} \tag{10}$$

where ρ_w and ρ_i are the dislocation densities in the walls and cell interiors, respectively. In Eq. (10), b is the magnitude of the dislocation Burgers vector, α is a constant (typically around 0.25) and μ is the shear modulus. Then, we make the classical assumption that the resolved shear strain rates for the cell walls $\dot{\gamma}_w$ and cell interiors $\dot{\gamma}_i$ are equal to some equivalent resolved shear strain $\dot{\gamma}$

$$\dot{\gamma}_w = \dot{\gamma}_i = \dot{\gamma}. \tag{11}$$

In addition, the equivalent resolved shear strain $\dot{\gamma}$ can be related to the plastic strain rate $\dot{\bar{\varepsilon}}$, using again the Taylor factor M:

$$\dot{\bar{\varepsilon}} = \frac{\dot{\gamma}}{M}. \tag{12}$$

The evolution of dislocations densities in this model is then accounted for by three contributions: dislocation nucleation, dislocation annihilation and migration of dislocations from cell interiors to cell walls. The evolution of dislocation densities in cell interiors ρ_i is described by the following equation

$$\dot{\rho}_i = \left(\alpha^* \frac{\sqrt{\rho}_w}{\sqrt{3}b} - \frac{6\beta^*}{bdv_i^{1/3}} - k_0\rho_i \right) M\dot{\bar{\varepsilon}}. \tag{13}$$

The first term corresponds to the contribution of Frank–Read sources in the nucleation of dislocation in cell interiors where α^* is constant related to the fraction of operative Frank–Read sources. The second term corresponds to the migration of dislocations from cell interiors to cell walls where β^* is a constant related to the fraction of dislocations moving from cell interiors to walls. The parameter d corresponds to the cell size. The third term describes the annihilation of dislocations where k_0 is a constant related to dislocation annihilation.

The evolution of dislocation densities in cell walls ρ_w is then described by the following equation

$$\dot{\rho}_w = \left(\alpha^* \frac{6v_i^{2/3}}{bdv_w} + \beta^* \frac{\sqrt{3}v_i\sqrt{\rho_w}}{v_w b} - k_0\rho_w \right) M\dot{\bar{\varepsilon}}. \tag{14}$$

In this equation, the first term is the contribution from the dislocation migrated from cell interiors to cell walls. The second term describes dislocation generated by activated Frank–Read sources and the third term corresponds to dislocation annihilation.

Motivated by experimental observation on metals (Estrin et al., 1998), the volume fraction of cell walls is assumed to decrease with the evolution of the resolved shear train according to the following phenomenological expression

$$v_w = v_{inf} + (v_0 - v_{inf})\exp\left(-\frac{M\bar{\varepsilon}}{\Gamma}\right), \tag{15}$$

where v_0 is the initial volume fraction of cell walls (before plastic deformation) and v_{inf} is the minimal value (reached after large plastic strains). In Eq. (15), Γ is a parameter that controls the "shrinkage" rate of the dislocation cells.

Finally, the total dislocation density in the material can be deduced from the dislocation densities in both cell walls and cell interior as

$$\rho = v_w\rho_w + v_i\rho_i. \tag{16}$$

Therefore, an increase of the dislocation density would lead to a decrease of the average grain size which can be estimated using Holt's equation:

$$d = \frac{K}{\sqrt{\rho}}, \tag{17}$$

where K is a material constant.

4. Numerical implementation of the model and preliminary applications

The numerical implementation of the model is now presented and in particular we focus on the local step of the elastoplastic solution which consists in projecting the elastic stress predictor on the yield surface.

4.1. Algorithm of solution

Following Enakoutsa et al. (2007) and Gurson (1977)'s model fits into the class of "generalized standard materials" (see also Bouby et al., 2023) under some hypotheses: the existence and uniqueness of the solution of the projection problem are ensured (Enakoutsa et al., 2007), provided that (i) the evolution equations of $\boldsymbol{\varepsilon}$ (the total strain) and $\bar{\varepsilon}$ (the hardening parameter) are discretized in time with an implicit-scheme; (ii) the additional terms due to the objective time-derivative of $\boldsymbol{\sigma}$ (in the hypoelasticity law) are discretized in time with an explicit-scheme; (iii) the value of the porosity f used in the criterion and the flow rule is taken at the preceding time-step.

The equations of the local projection problem to be solved[1] are

$$\begin{cases} \boldsymbol{\varepsilon} = \boldsymbol{\varepsilon}^e + \boldsymbol{\varepsilon}^p & \text{Decomposition of the total strain} \\ \boldsymbol{\sigma} = (3\kappa\mathbb{J} + 2\mu\mathbb{K}) : \boldsymbol{\varepsilon}^e & \text{Isotropic elasticity law} \\ \Phi(\boldsymbol{\sigma}, f, \bar{\sigma}) \le 0 & \text{Plasticity criterion} \\ \begin{cases} \dot{\boldsymbol{\varepsilon}}^p &= \dot{\lambda}\dfrac{\partial\Phi}{\partial\boldsymbol{\sigma}}(\boldsymbol{\sigma}, f, \bar{\sigma}) \\ \dot{\lambda} &\ge 0 \\ \dot{\lambda}\Phi(\boldsymbol{\sigma}, f, \bar{\sigma}) &= 0 \end{cases} & \text{Flow rule and consistency conditions} \\ \dot{\bar{\sigma}} \equiv \sigma(\bar{\varepsilon}, \rho_w, \rho_i), (1-f)\dot{\bar{\sigma}\bar{\varepsilon}} = \boldsymbol{\sigma} : \dot{\boldsymbol{\varepsilon}}^p, & \text{Strain hardening law} \end{cases} \tag{18}$$

where $\bar{\sigma} \equiv \sigma(\bar{\varepsilon}, \rho_w, \rho_i)$ is the hardening function depending on the dislocation densities of the composite microstructure, $\boldsymbol{\varepsilon}^e$ is the elastic strain tensor, $\boldsymbol{\varepsilon}^p$ the plastic strain tensor. The fourth-order tensors $\mathbb{J}$ and $\mathbb{K}$ are respectively the spherical projection tensor and the deviatoric projection tensor, and κ and μ are respectively the bulk and shear moduli.

The local projection problem thus consists in finding the mechanical state $S_{n+1} = \left\{\boldsymbol{\varepsilon}_{n+1}, \boldsymbol{\varepsilon}^p_{n+1}, \boldsymbol{\sigma}_{n+1}, \bar{\varepsilon}_{n+1}\right\}$ at time t_{n+1} resulting from a given, known strain increment $\Delta\boldsymbol{\varepsilon}_n$ (resulting from a global elastoplastic iteration), knowing the previous mechanical state $S_n = \left\{\boldsymbol{\varepsilon}_n, \boldsymbol{\varepsilon}^p_n, \boldsymbol{\sigma}_n, \bar{\varepsilon}_n\right\}$ at time t_n. The yield criterion and the flow rule are thus discretized using an implicit scheme with respect to $\boldsymbol{\varepsilon}^p$ and $\bar{\varepsilon}$, while an explicit scheme is considered for f. The discretized equations of the local projection problem are given by

$$\begin{cases} \boldsymbol{\sigma}_{n+1} &= \boldsymbol{\sigma}^{\text{elas}}_{n+1} - (3\kappa\mathbb{J} + 2\mu\mathbb{K}) : \Delta\boldsymbol{\varepsilon}^p_n \\ \Phi(\boldsymbol{\sigma}_{n+1}, f_n, \bar{\sigma}_{n+1}) &\le 0 \\ \Delta\boldsymbol{\varepsilon}^p_n &= \Delta\lambda_n\dfrac{\partial\Phi}{\partial\boldsymbol{\sigma}}(\boldsymbol{\sigma}_{n+1}, f_n, \bar{\sigma}_{n+1}) \\ \Delta\lambda_n &\ge 0 \\ \Delta\lambda_n\Phi(\boldsymbol{\sigma}_{n+1}, f_n, \bar{\sigma}_{n+1}) &= 0 \\ \bar{\sigma}_{n+1} &= \sigma(\bar{\varepsilon}_n + \Delta\bar{\varepsilon}_n) \\ (1-f_n)\bar{\sigma}_{n+1}\Delta\bar{\varepsilon}_n &= \boldsymbol{\sigma}_{n+1} : \Delta\boldsymbol{\varepsilon}^p_n, \end{cases} \tag{19}$$

where $\boldsymbol{\sigma}^{\text{elas}}_{n+1} = \boldsymbol{\Sigma}_n + (3\kappa\mathbb{J} + 2\mu\mathbb{K}) : \Delta\boldsymbol{\varepsilon}_n$ is the elastic predictor, that is the stress tensor at time t_{n+1} resulting from the strain increment $\Delta\boldsymbol{\varepsilon}_n$ fictitiously considered as purely elastic.

The algorithm consists essentially in finding $\bar{\sigma}_{n+1}$ and $\Delta\lambda_n$ and the treatment of hardening is done classically using a fixed point method, as explained in the following steps:

[1] As explained by Enakoutsa et al. (2007), large displacements and strains do not modify the properties of generalized standard materials, provided that the equilibrium equations are solved on the current configuration and the (hypo)elasticity law include corrections so as to respect objectivity. The algorithm will thus simply be presented in small strain by replacing the Eulerian strain rate by the time-derivative of the linearized strain $\boldsymbol{\varepsilon}$.

(1) Initialization of the yield stress using the previous value. Assume that

$$\begin{cases} \rho_{w,n+1} &= \rho_{w,n} \\ \rho_{i,n+1} &= \rho_{i,n} \\ v_{w,n+1} &= v_{inf} + (v_0 - v_{inf})\exp\left(-\dfrac{\bar{\varepsilon}_n}{\Gamma}\right) \\ v_{i,n+1} &= 1 - v_{w,n+1} \\ d_{n+1} &= \dfrac{K}{\sqrt{v_{w,n+1}\rho_{w,n+1} + v_{i,n+1}\rho_{i,n+1}}} \end{cases}. \tag{20}$$

so one has

$$\bar{\sigma}_{n+1} = \bar{\sigma}_n = \frac{\alpha\mu b}{M}(v_{w,n+1}\sqrt{\rho_{w,n+1}} + v_{i,n+1}\sqrt{\rho_{i,n+1}}). \tag{21}$$

(2) Compute $\Delta\lambda_n$ with this value $\bar{\sigma}_{n+1}$ and then deduce ε^p_{n+1} and σ_{n+1}. This step will not be detailed here since it is quite standard for the GTN model and can be done using a Newton method on a single unknown (see e.g. the algorithms of Enakoutsa et al., 2007 or Bouby et al., 2023).

(3) Deduce the increment of equivalent accumulated plastic strain $\Delta\bar{\varepsilon}_n = \dfrac{\sigma_{n+1} : \Delta\varepsilon^p_n}{(1-f_n)\bar{\sigma}_{n+1}}$.

(4) Compute the increment of dislocation densities

$$\begin{cases} \Delta\rho_{w,n} &= \left(\alpha^* \dfrac{6(v_{i,n+1})^{2/3}}{bd_{n+1}v_{w,n+1}} + \beta^* \dfrac{\sqrt{3}v_{i,n+1}\sqrt{\rho_{w,n+1}}}{v_{w,n+1}b} - k_0\rho_{w,n+1}\right) M\Delta\bar{\varepsilon}_n \\ \Delta\rho_{i,n} &= \left(\alpha^* \dfrac{\sqrt{\rho}_{w,n+1}}{\sqrt{3}b} - \dfrac{6\beta^*}{bd_{n+1}v_{i,n+1}^{1/3}} - k_0\rho_{i,n+1}\right) M\Delta\bar{\varepsilon}_n. \end{cases} \tag{22}$$

(5) Update the values of the dislocation densities, volume fraction of cell walls and average cell size

$$\begin{cases} \rho_{w,n+1} &= \rho_{w,n} + \Delta\rho_{w,n} \\ \rho_{i,n+1} &= \rho_{i,n} + \Delta\rho_{i,n} \\ v_{w,n+1} &= v_{inf} + (v_0 - v_{inf})\exp\left(-M\dfrac{\bar{\varepsilon}_n + \Delta\bar{\varepsilon}_n}{\Gamma}\right) \\ v_{i,n+1} &= 1 - v_{w,n+1} \\ d_{n+1} &= \dfrac{K}{\sqrt{v_{w,n+1}\rho_{w,n+1} + v_{i,n+1}\rho_{i,n+1}}}. \end{cases} \tag{23}$$

(6) Deduce a refined estimate of $\bar{\sigma}_{n+1}$:

$$\bar{\sigma}_{n+1} = \frac{\alpha\mu b}{M}(v_{w,n+1}\sqrt{\rho_{w,n+1}} + v_{i,n+1}\sqrt{\rho_{i,n+1}}). \tag{24}$$

and follow the procedure (step 2 to 6) until the method converges and $\bar{\sigma}_{n+1}$ reaches a stationary value.

This algorithm has been implemented as a UMAT (user-material) subroutine in the finite element solver ABAQUS.

4.2. Calibration of material parameters

The model parameters have been calibrated for the pure copper considered in the experiments of Section 2. First, the elastic constant for the pure copper are classically taken as $E = 120$ GPa and $\nu = 0.358$.

Then, the parameters related to the hardening composite model are calibrated by adjusting the parameters found in the literature (Lapovok et al., 2005; Gu et al., 2012) and previously calibrated using TEM for initial dislocation densities (ρ_w and ρ_i), EBSD for volume fraction of cell walls and interiors (v_w and v_i) and discrete dislocation dynamics simulations for dislocation nucleation, migration and annihilation constants (α^* and β^* and k_0), in order to reproduce the experimental stress–strain curve of the tensile test for the pure copper. The set of parameters related to hardening is provided in Table 1.

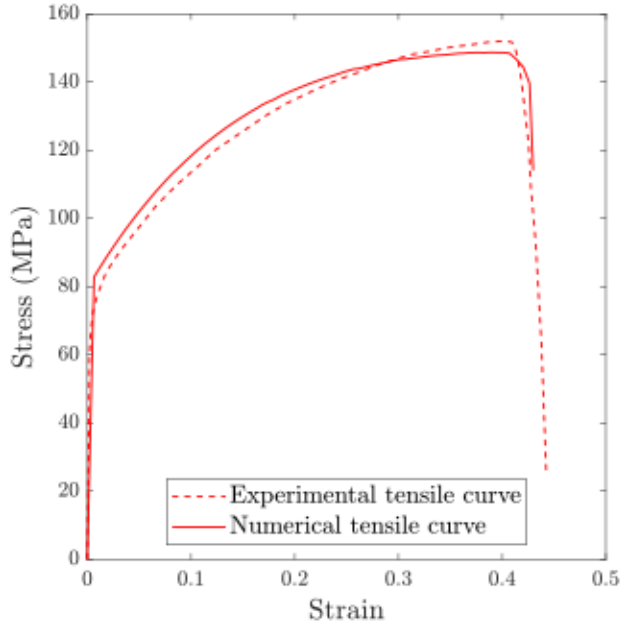

Fig. 7. Comparison of numerical and experimental stress–strain curves for pure copper.

Finally, the next step is the calibration of the GTN damage parameters (f_0, f_c, δ, f_N, s_N and ε_N). This can be done through microtomography observations using synchrotron diffraction experiments (see e.g. Thuillier et al., 2012) or by using macroscopic results such as a tensile test. Here the parameters have been calibrated using the macroscopic tensile test for simplicity. The set of parameters related to damage is provided in Table 2.

The model predictions (using the calibrated parameters) are compared to the experimental results in Fig. 7. Overall the numerical stress–strain curve is in a good agreement with the experimental curve.

4.3. Preliminary application to the study of grain refinement in an axisymmetric proportional loading example

As a preliminary application of the model, we investigate the response of an elementary volume for an axisymmetric proportional loading with major axial stress, under conditions of fixed stress triaxiality. This case of homogeneous loading will be of interest to study the influence of the initial porosity and loading conditions on the achievable grain refinement before failure. Therefore, it will be applied to several fictitious materials with different initial porosities.

We consider an elementary volume (i.e. a material point) subjected to a macroscopic loading state under conditions of fixed stress triaxiality $T = \sigma_m/\sigma_{eq}$. The non-zero components of the stress tensor are:

$$\sigma_{11} = \sigma_{22} = \sigma_m - \frac{1}{3}\sigma_{eq}, \quad \sigma_{33} = \sigma_m + \frac{2}{3}\sigma_{eq}. \tag{25}$$

In terms of model parameter, we take the calibrated values of the hardening behavior of the pure copper given in Table 2. For the parameters of the GTN model, we will consider fictitious values for the porosity (in order to study its influence) and no nucleation will be considered: we will take the values $f_0 = [0.0002;\ 0.001;\ 0.005]$ and $f_c = 0.01$. In addition, several values for the stress triaxialitiy will be considered: $T = [1/3;\ 1/2;\ 2/3;\ 3/4;\ 1;\ 3/2]$. The objective of these simulations is to investigate the influence of the porosity f_0 and the loading conditions (through the value of the imposed stress triaxiality T) on grain refinement. In particular, we will study the evolution of the grain size d (as a function of the strain), and notably the value of $d_{\min}$ when coalescence is reached: this value simply corresponds to the

Table 1
Values of parameters for dislocation density based hardening law for pure copper.

ρ_{w0} [m^{-2}]	ρ_{i0} [m^{-2}]	α	b [m]	M	α^*	β^*	k_0	$v_{w,f}$	v_0	Γ	K
4×10^{14}	2×10^{14}	0.25	2.56×10^{-10}	3.06	0.065	0.012	4.3	0.06	0.2	3.2	500

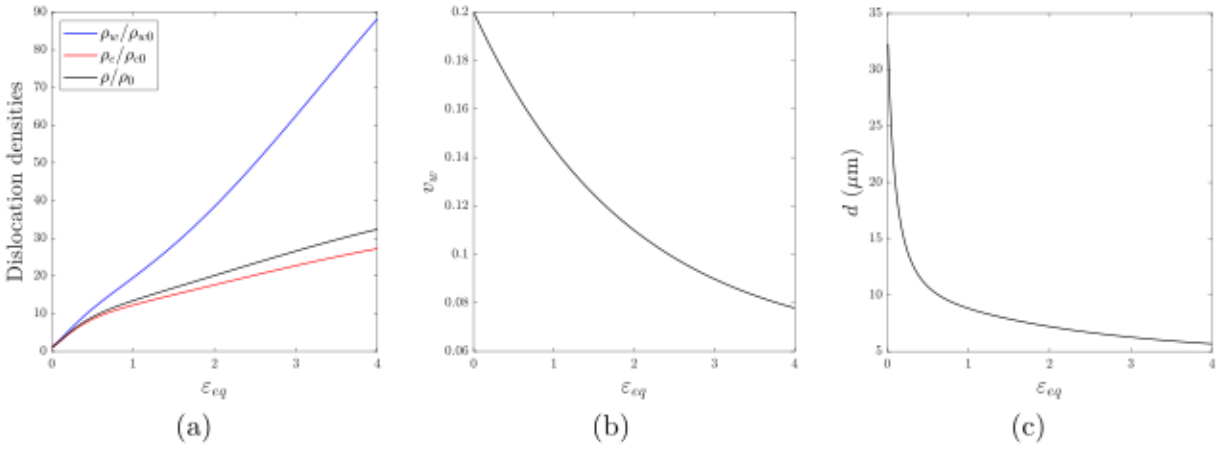

Fig. 8. Evolution of several internal model parameters for $T = 1/3$ and $f_0 = 0.0002$. (a) Normalized dislocation densities in cell walls ρ_w/ρ_{w0}, cell interiors ρ_i/ρ_{i0} and total dislocation density ρ/ρ_0, (b) Volume fraction of cell walls v_w and (c) Average cell size parameter d.

minimal grain size achievable before failure. Therefore the maximum grain refinement before coalescence is given by the ratio $d_0/d_{\min}$.

First, for illustrative purposes, the evolution of several internal parameters is shown in Fig. 8 in the case $T = 1/3$ and $f_0 = 0.0002$. The evolution of the normalized dislocation densities in cell walls ρ_w/ρ_{w0} and cell interiors ρ_i/ρ_{i0} are shown in Fig. 8a. The increase of the dislocation density in the walls is very important in comparison to the increase of the dislocation in the cell interiors. However, it has only a moderate effect on the evolution of the total dislocation density ρ/ρ_0 because the volume fraction of cell walls v_w is initially lower than that of cell interiors v_i and it decreases rapidly as shown in Fig. 8b. The average cell size d is then represented in Fig. 8c: it decreases from the value $d_0 \sim 32$ μm to approximately $d_{\min} \sim 5.7$ μm (at $\varepsilon_{eq} \sim 4$): therefore in that case a "grain refinement" with a ratio $d_0/d_{\min} \sim 5.6$ is achieved.

Finally, the maximum cell refinement $d_0/d_{\min}$ before the coalescence occurrence, is represented in Fig. 9 for all the values of f_0 and T considered. As expected, grain refinement is promoted by a decrease of the triaxiality and the initial volume fraction f_0; it should be noted that the values considered for the triaxiality has been restricted to $T > 1/3$ because the GTN model is not suitable at low stress triaxiality (requiring a proper modeling of void shape effects). Nonetheless, the trend observed is expected to continue when T reaches zero to negative values but eventually a threshold for d_0/d is also expected to exist. According to these results, an important grain refinement can be achieved at low stress triaxiality levels and with materials having low levels of initial pororities. In the context of SPD processes, in which the final aim is to provide important grain refinement, these results show that grain refinement is generally influenced by (i) the initial conditions of the material in term of damage and (ii) the loading conditions applied to the material during the process.

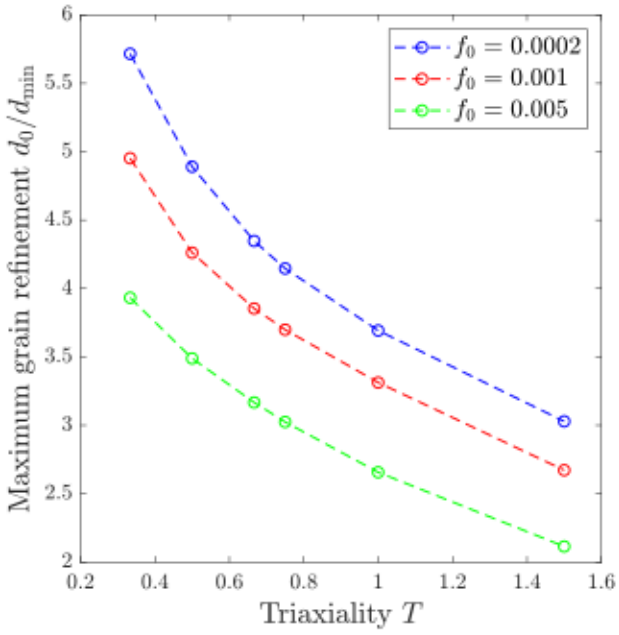

Fig. 9. The maximum grain refinement $d_0/d_{\min}$ achieved as a function of the stress triaxiality T for several initial void volume fractions f_0.

Table 2
Values of parameters for damage in the case of pure copper.

f_0	q	f_c	δ	f_N	ε_N	s_N
0.001	1	0.01	8	0.01	0.3	0.2

5. Application to the prediction of the stress–strain curves after processing by repetitive corrugation and straightening

We now study numerically the evolution of the parameters describing strength and ductility during the RCS process presented in Section 2, with notably the objective of predicting the stress–strain curve after processing (in order to investigate the evolution of the strength and ductility after a severe plastic deformation process).

5.1. Description of the numerical model

A 3D finite element model of the RCS process has been made using the commercial code ABAQUS/Standard. Following Tajdary et al. (2021) (see also Tajdary et al., 2022), the simulation of multi-pattern RCS can be performed on a single elementary pattern subjected to symmetric and periodic boundary conditions (depending on the loading step). The numerical model used for investigating the strength-ductility

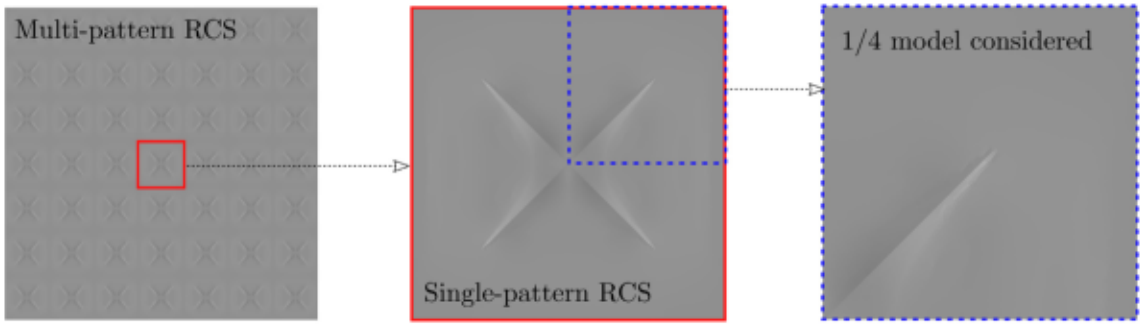

Fig. 10. Geometry considered in the simulation of RCS.

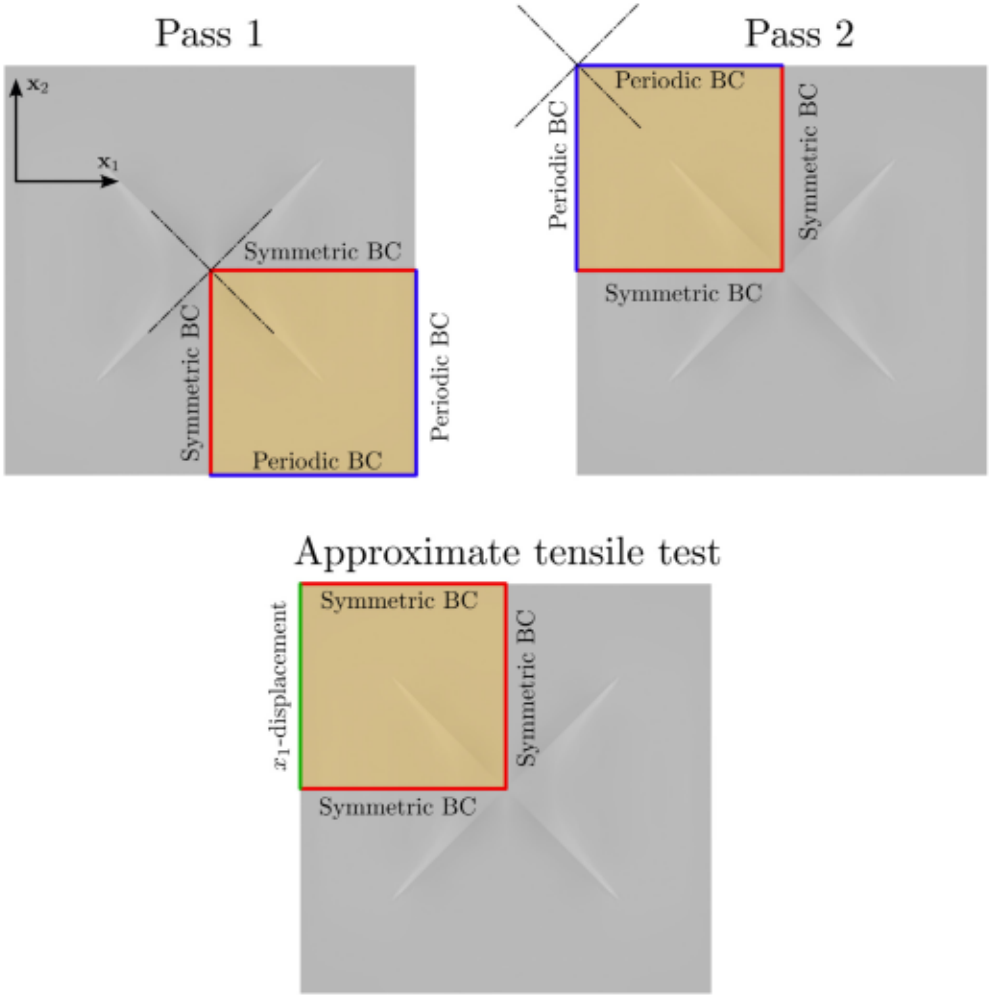

Fig. 11. Boundary conditions considered for the simulations.

trade-off is then composed of a two passes RCS procedure followed by a tensile test. The simulation of RCS is composed of one deformable sheet metal blank, four corrugation and four straightening dies. Due to the symmetry of the problem only 1/4 of a single pattern is considered (see Fig. 10). The sheet metal is modeled as a 3D deformable part and we use selectively subintegrated 8-node trilinear brick (C3D8 elements in ABAQUS) which are suitable for quasi-incompressible plasticity. A mesh size of 0.1 mm has been used for the deformable sheet metal and 0.15 mm for the rigid dies. Also the coefficient of friction is taken equal to 0.05 which represents low friction (due to Teflon) copper-steel contact. The corrugation and straightening dies are modeled as rigid 3D shells.

In order to perform the second pass, the sheet metal is turned upside-down and the corrugation dies are moved half a pattern (8 mm) in both the x_1- and x_2-directions. The boundary conditions that are applied on the boundaries of the specimen are represented in Fig. 11. After the very last step of the second pass, a tensile test is performed: this is done by applying a displacement on the surface of the blank in the x_1 direction while maintaining the double symmetry conditions on surfaces with normal vectors x_1 and x_2 (see Fig. 11). It should be noted

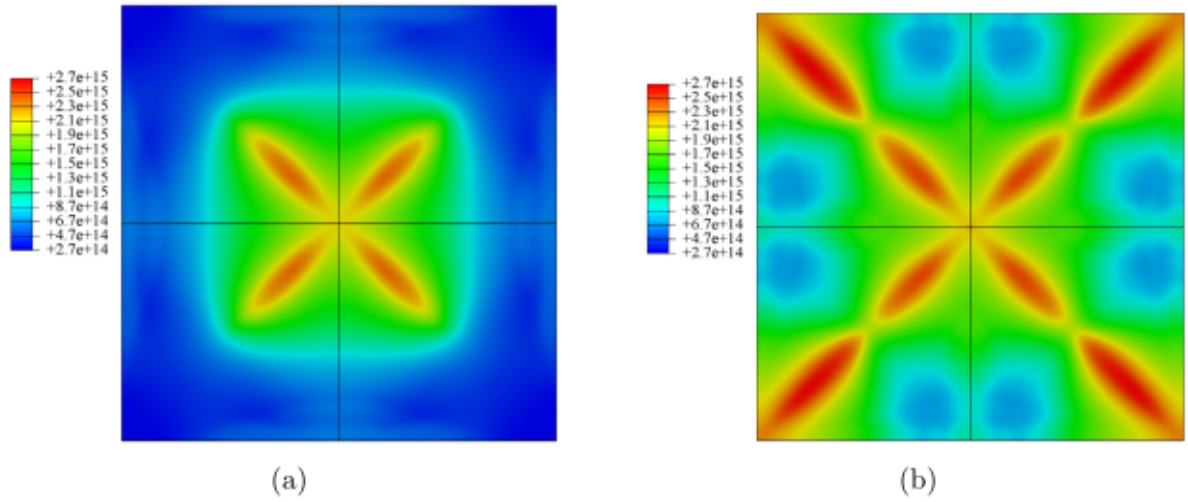

Fig. 12. Distribution of total dislocation density ρ (in m^{-2}) after (a) Pass 1 and (b) Pass 2. The value before processing is $\rho_0 = 2.4 \times 10^{14}$ m^{-2}.

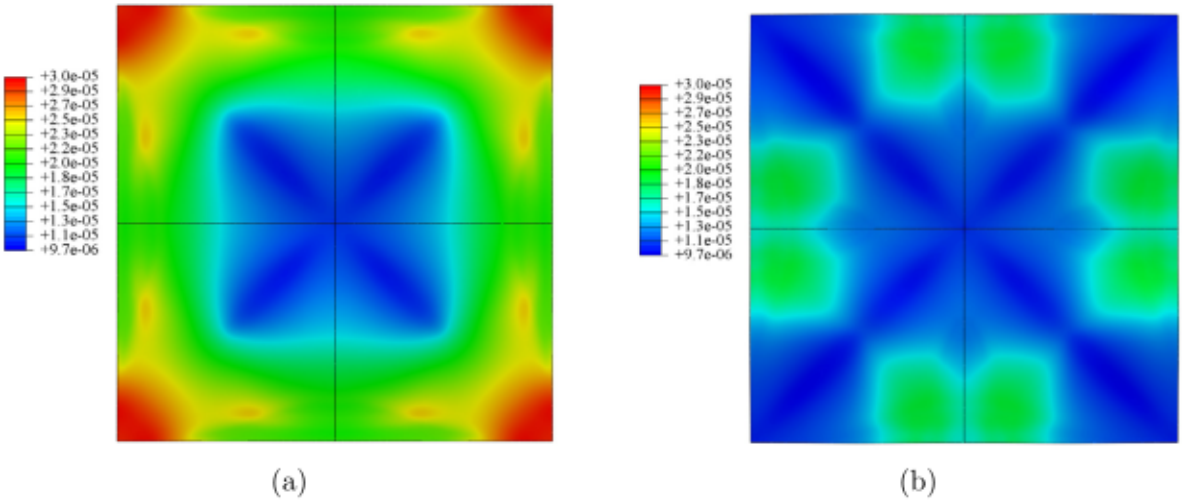

Fig. 13. Distribution of average cell size d (in m) after (a) Pass 1 and (b) Pass 2. The value before processing is $d_0 = 32.3$ μm.

that this procedure permits only to perform an approximate tensile test, as necking cannot take place.

Several quantities will be studied in order to investigate the evolution of damage and dislocation structure as a function of the number of RCS passes:

(1) The distribution of internal variables of the model will be studied after 1 and 2 passes. In particular we will consider variables related to (i) hardening such as total dislocation density ρ and average cell size d and (ii) damage void volume fraction f. This allows us to better understand the phenomenon governing the change in strength and ductility happening during RCS.
(2) The macroscopic stress–strain response before and after the process will be studied. This will show the increase in the strength and the evolution of the ductility after each pass.

5.2. Microscopic results

First, we study the distribution of the total dislocation density ρ, represented in Fig. 12 after pass 1 and pass 2. (Initially it is homogeneous with a value $\rho_0 = 2.4 \times 10^{14}$ m^{-2}). After the first pass, the maximum value of the dislocation increases by a factor of 10 from an initial value of 2.4×10^{14} m^{-2} to 2.4×10^{15} m^{-2}. It is very heterogeneous with a minimum value of 2.7×10^{14} m^{-2} (in the areas far from the corrugation pattern) and a maximum value of 2.4×10^{15} m^{-2}. Its average value (which can be computed by volume averaging) is of about 9×10^{14} m^{-2}. After the second pass, the distribution of ρ is more homogeneous, with a minimum value of 6.8×10^{14} m^{-2} and a maximum value of 2.7×10^{15} m^{-2}. In this case, its average value is of about 1.5×10^{15} m^{-2}. Therefore, both the maximum and average of the total dislocation density increase with the number of pass. In addition, the homogeneity of the distribution also increases with the number of passes.

Fig. 13 illustrates the distribution of average cell (grain) size parameter d after pass 1 and pass 2. (Initially it is homogeneous with a value $d_0 = 32.3$ μm). After the first, a moderate grain refinement by a factor of 3 has been achieved, mainly in the heavily deformed parts of the specimen: the minimum and maximum grain sizes are respectively of about 10 and 32 μm, and the average grain size is 18 μm. After the second pass, the minimum grain size does not change much (from 10 to 9 μm), but the homogeneity of the refinement increases. Indeed in that case, the minimum and maximum grain sizes are respectively of about 9 and 19 μm, and the average grain size is 13 μm. This increase in the homogeneity of the grain size is mainly due to the shift of the corrugation dies between the first and the second pass.

Then, in order to follow the evolution of damage during the process, Fig. 14 shows the distribution of the void volume fraction f after pass 1

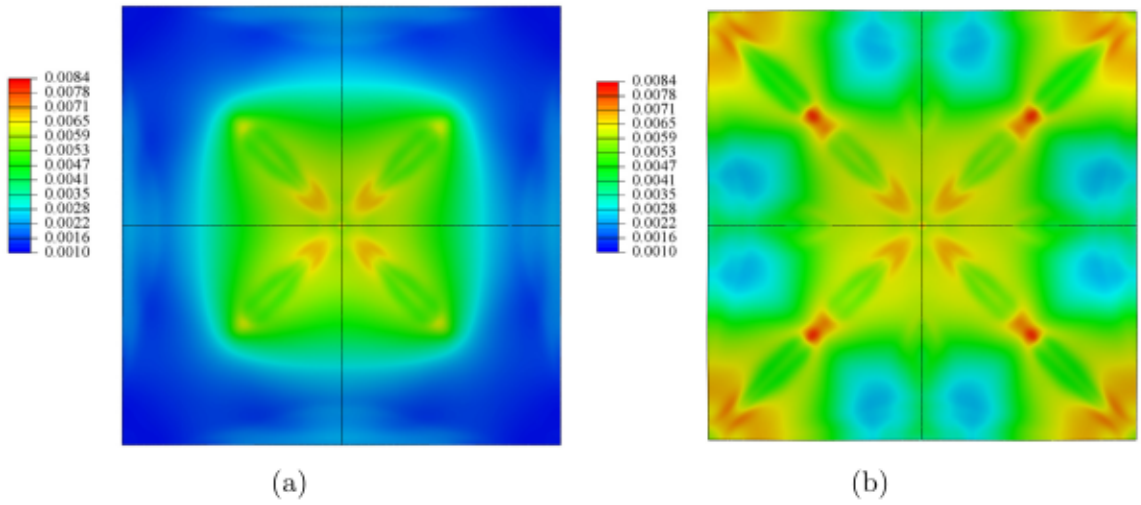

Fig. 14. Distribution of the void volume fraction f after (a) Pass 1 and (b) Pass 2. The value before processing is $f_0 = 0.001$.

and pass 2. (Initially it is homogeneous with a value $f_0 = 0.001$). After the first pass, the distribution of the porosity is very heterogeneous, as it reaches a maximum value of 0.006 in a very localized area in the cross-shaped zone at the back side of the sheet metal. After the second pass, the maximum value is shifted to the position of the new cross and reaches a value of 0.009 (located on the front side of the specimen). It is also heterogeneous with maximum values localized in very small areas. It should be noted that the evolution of void volume fraction is mainly due to the corrugation step: the maximum value of f in corrugation steps of pass 1 and pass 2 has reached 0.009 and 0.02 (and then it decreases during straightening). Overall, the void volume fraction increases moderately during a full pass but it becomes quite heterogeneous, which may modifies considerably the ductility.

5.3. Macroscopic results: prediction of strength and ductility

The stress–strain curves predicted numerically before and after processing are represented in Fig. 15 and compared to the experimental results. First, before processing, a very good agreement is observed between the numerical and experimental results which is expected as the model parameters have been actually calibrated to reproduce this case. Then, the stress–strain curve predicted numerically after the second pass is qualitatively in good agreement with the experimental results both in terms of ductility and strength. In the numerical simulation, failure is observed by a numerical instability with an abrupt softening corresponding to a vertical slope of the force–displacement curve. The strain to failure and the tensile strength simulated numerically after processing are in agreement with the experimental results. The strength predicted numerically is slightly overestimated but overall, the evolution of hardening is well reproduced, in particular by comparison with the behavior before processing. It should be noted that the experimental stress–strain curve after one pass is not included due to the lack of repeatability of the results when the tensile specimen is cut from different parts of the processed sheet metal.

A quantitative comparison between the numerical and experimental results is then done by extracting from the stress–strain curves the main strength-ductility properties: the yield strength $R_{p0.2}$, the tensile strength R_m and the elongation El (maximal strain). The effect of processing on the strength-ductility properties is then represented in the planes $(El, R_{p0.2})$ and (El, R_m), in Fig. 16. Overall, these results quantitatively confirm that processing by RCS decreases the ductility but increase both the yield strength $R_{p0.2}$ and the tensile strength

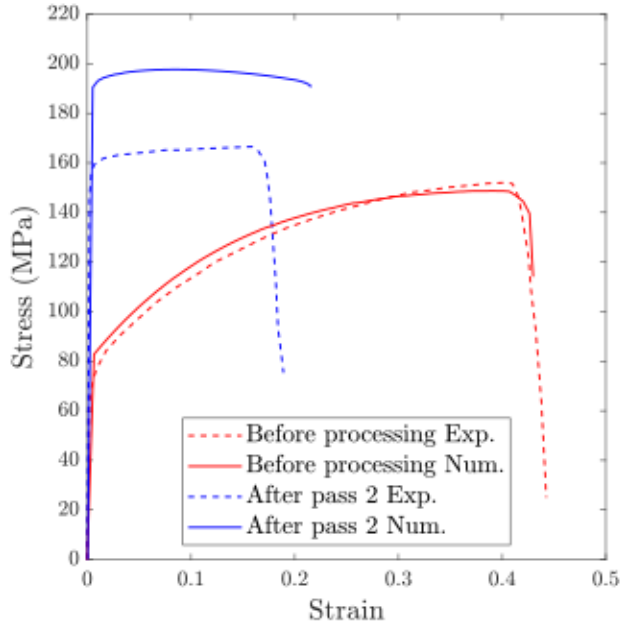

Fig. 15. Comparison of numerical and experimental stress–strain curves for copper.

R_m. It is interesting to note that, for the yield strength $R_{p0.2}$, the difference observed initially between the numerical and experimental results before processing is less amplified in comparison with the tensile strength R_m; this means that for this quantity, the predictions of the model calibrated before processing are not degraded as the model capture the main effects of processing. In terms of the tensile strength, the difference observed initially between the numerical and experimental results before processing are more amplified after processing but overall the effect of processing is qualitatively captured.

6. Discussion

The model developed in this work allows a description of several microstructural changes that occur during plastic deformation such as the evolution of the dislocation density, grain size and void volume fraction, supposedly responsible for the modification of strength and

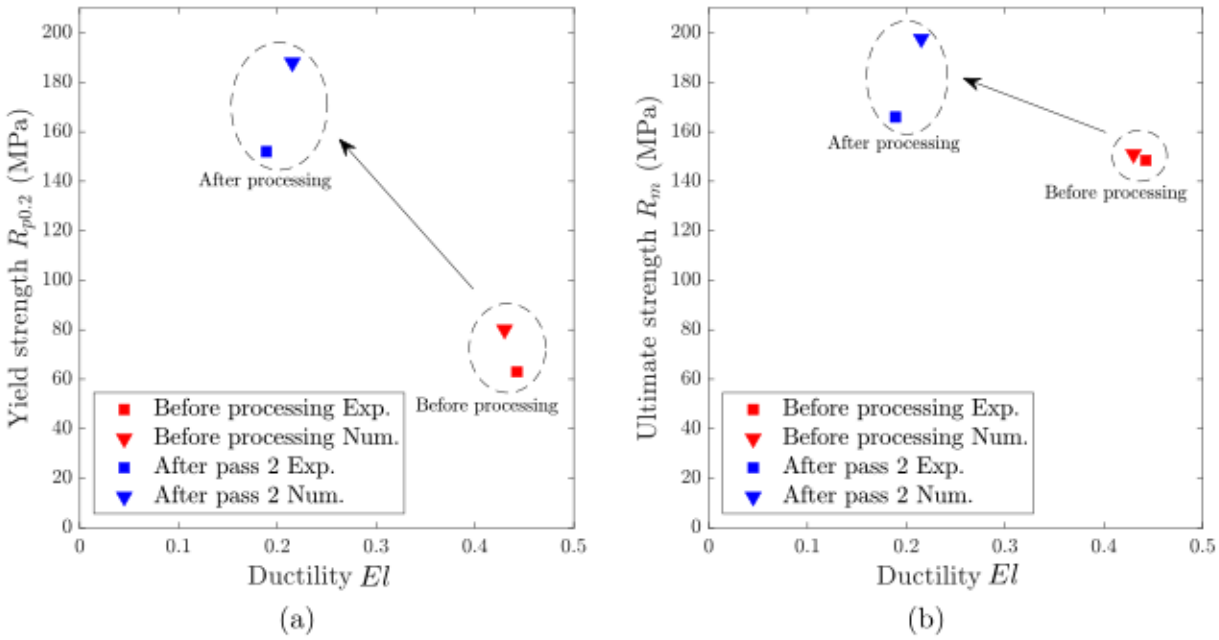

Fig. 16. Strength-ductility properties before and after processing. (a) Yield strength $R_{p0.2}$ and (b) Tensile strength R_m.

ductility. The model has been used to simulate a multi-pass SPD process and overall it has been successful in predicting the strength-ductility trade-off after plastic deformation. Several comments are in order:

- The numerical tensile test performed after the second pass of RCS may not be fully representative of the experimental tensile test because it is performed on a single pattern (with periodic boundary conditions) while the specimen for the experimental tensile test has been performed using a standard geometry; necking is thus absent from the numerical simulation. It should also be noted that the experimental results can be different if the specimen is cut in another location of the processed specimen: the location and the pattern chosen to cut the specimen can (slightly) influence the stress–strain curve. For instance, the RCS experimental geometry is composed of a 7×7 corrugation die pattern, so a specimen cut from the exterior patterns would not provide representative results (see Tajdary et al., 2021). Furthermore it was observed that after one pass, there is a lack of representativity of the experimental stress–strain curves because of the process is very heterogeneous after one pass.
- Another source of differences between the simulated and experimental tensile tests is related to the prediction of the material state, in terms of damage levels and dislocation densities, after the process. Indeed, the distribution of damage and dislocation density may not be fully representative of the experimenal results because, as shown by Ezequiel et al. (2020b), the numerical simulation of this process is very sensitive to the process parameters (friction coefficient, die force, etc.) but also the boundary conditions applied on the elementary pattern considered (Tajdary et al., 2021).
- The porosity increases in corrugation step and decreases in straightening due to high compression. However the increase is not completely reversible because the "nucleated porosity" continues increasing at each pass. Consequently, the void volume fraction evolution has an irreversible cyclic characteristic and the highest value is always achieved at the corrugation step. Depending on the material, fracture can even eventually happen during corrugation as shown by Tajdary et al. (2022) in the case of an aluminum alloy AA7075. This irreversible behavior explains how damage will modify ductility after processing. Indeed, after processing the total porosity in the material is higher than in the initial state due to continuous increase of the porosity due to nucleation, which would ultimately decrease the overall ductility.
- The model developed in this work was based on the GTN model (for spherical voids) because of the relatively high triaxiality during RCS processing with low levels of corrugations (as shown by Tajdary et al., 2022). This model is only valid as long as we avoid inducing shear deformation by applying high values of corrugation die displacement. It should be mentioned that void shape effects have a moderate influence in this process so that neglecting them could delay the onset of fracture to some extent (Tajdary et al., 2022). The extension of this work to void shape effects, by considering for instance the Madou–Leblond model (Madou and Leblond, 2012a,b), would permit to consider shear-dominated loadings and thus improve the prediction of damage in areas of the specimen subjected to low-stress triaxiality levels. However since coalescence under shear is complex, the prediction of the ductility would still be difficult as the modeling of coalescence within the Madou–Leblond model generally requires adjustable parameters with the triaxiality (Morin et al., 2016, 2017a).
- As the model developed in this work is based on the GTN model which is derived using limit-analysis, it excludes by essence rate-dependent behaviors. Since in practice the hardening model of Estrin et al. (1998) is rate-dependent (to describe dynamic recovery notably), it could be interesting to refine the model by considering a rate-dependent extension of Gurson's model, as done by Pan et al. (1983) and Leblond et al. (1994).
- Deformation twinning was not included in the plasticity model. In the GTN framework, this requires to take into account a single crystal plasticity model in the matrix during the upscaling procedure which raises important difficulties in the limit-analysis procedure (see e.g. Paux et al., 2015). Therefore, twinning deformation is generally disregarded in micromechanical models of ductile failure.

7. Conclusion

The aim of this work was to analyze experimentally and numerically the modifications of both strength and ductility after processing by

severe plastic deformation. Tensile tests have been performed on a pure copper sample before and after two passes of repetitive corrugation and straightening; processing by plastic deformation decreases the ductility but increases the strength. An extended Gurson model including dislocation density evolution was developed and implemented numerically, in order to take into account the cellular microstructure of materials processed by severe plastic deformation. The model has been first applied to the study of grain refinement in an axisymmetric proportional loading example, allowing the investigation of the maximum grain refinement as a function of the triaxiality and initial porosity. Finally the model was applied to the prediction of the strength and ductility of a specimen processed by RCS after two passes. The summary of findings is as follows:

- In the case of axisymmetric proportional loading, the maximum grain refinement predicted by the extended Gurson model is directly influenced by the initial material degradation state (initial void volume fraction) and the loading condition (stress triaxiality): decreasing the stress triaxiality and the initial porosity allows achieving more grain refinement before the onset of coalescence.
- The simulation of two pass RCS with this extended Gurson model enabled us to have access to the evolution of internal parameters responsible for the modifications in strength and ductility after each pass. The strength-ductility trade-off has been investigated within a virtual design approach and was shown to depend on (i) the evolution of the hardening parameters and (ii) the continuous increase of the porosity during processing.
- The good agreement observed between the experimental and numerical results in terms of modification of strength and ductility suggests that considering a physically-based model of hardening and a micromechanical model of ductile damage is sufficient to describe qualitatively (and quantitatively to some extent) the strength-ductility trade-off.

The model developed can be used as a viable alternative to Voce or Swift type hardening models in Gurson's approach as it is valid for high strain deformations usually experienced during SPD. Furthermore it can be used to follow locally the evolution of the microstructure (and therefore can be compared to experimental data such as EBSD maps). This model constitutes a first step toward a quantitative prediction of the strength-ductility trade-off because it is still restricted to moderate triaxiality levels and the modeling of coalescence is heuristic. Further developments of this approach should include (i) void shape effects that are important at low stress triaxiality and (ii) a micromechnical modeling of coalescence in order to capture more precisely strain localization as a measure of ductility.

CRediT authorship contribution statement

Pouya Tajdary: Writing – review & editing, Writing – original draft, Methodology, Investigation, Conceptualization. **Léo Morin:** Writing – review & editing, Writing – original draft, Supervision, Methodology, Investigation, Conceptualization. **Chedly Braham:** Writing – review & editing, Writing – original draft, Supervision, Methodology, Investigation, Conceptualization. **Omar Novelo Peralta:** Investigation. **Gonzalo Gonzalez:** Writing – review & editing, Writing – original draft, Supervision, Methodology, Investigation, Conceptualization.

Declaration of competing interest

The authors declare that they have no known competing financial interests or personal relationships that could have appeared to influence the work reported in this paper.

Data availability

Data will be made available on request.

Acknowledgments

G.G. acknowledges the funding support from UNAM-DGAPA-PAPIIT through projet IN102321. The authors acknowledge Alan Raúl Gomez Rico and Gabriel Angel Lara Rodriguez for providing experimental data that serves as input to model calculations.

References

Alvarado, E.E., Figueroa, I.A., Gonzalez, G., 2020. Microstructural and mechanical analysis of an 1100 aluminum alloy processed by repetitive corrugation and straightening. Phys. Met. Metallogr. 121, 1319–1325.
Benzerga, A.A., Leblond, J.B., Needleman, A., Tvergaard, V., 2016. Ductile failure modeling. Int. J. Fract. 201, 29–80.
Bhovi, P.M., Gururaj, S.H., Lohit, R.B., Venkateswarlu, K., 2018. Simulation studies on RCS processed Al-Mg-Sc alloy. Mater. Today: Proc. 5, 7525–7531.
Bhovi, P.M., Patil, D.C., Kori, S.A., Venkateswarlu, K., Huang, Y., Langdon, T.G., 2016. A comparison of repetitive corrugation and straightening and high-pressure torsion using an Al-Mg-Sc alloy. J. Mater. Res. Technol. 5, 353–359.
Bouby, C., Morin, L., Bignonnet, F., Dormieux, L., Kondo, D., 2023. On the thermodynamics consistency of Gurson's model and its computational implications. Int. J. Solids Struct. 279, 112359.
Chen, Z., Sun, Z., Panicaud, B., 2019. Investigation of ductile damage during surface mechanical attrition treatment for TWIP steels using a dislocation density based viscoplasticity and damage models. Mech. Mater. 129, 279–289.
Chu, C.C., Needleman, A., 1980. Void nucleation effects in biaxially stretched sheets. J. Eng. Mater. Technol. 102, 249–256.
Elizalde, S., Ezequiel, M., Cabrera, J.M., Figueroa, I.A., Baile, M.T., Gonzalez, G., Elizalde, S., Ezequiel, M., Cabrera, J.M., Figueroa, I.A., Baile, M.T., Gonzalez, G., 2021. Study on the formability and texture evolution of AA6061 alloy processed by repetitive corrugation and straightening. J. Appl. Res. Technol. 19, 548–561, Publisher: Universidad Nacional Autónoma de México, Instituto de Ciencias Aplicadas y Tecnología..
Elizalde, S., Ezequiel, M., Figueroa, I.A., Cabrera, J.M., Braham, C., Gonzalez, G., 2020. Microstructural evolution and mechanical behavior of an Al-6061 alloy processed by repetitive corrugation and straightening. Metals 10 (489).
Enakoutsa, K., Leblond, J., Perrin, G., 2007. Numerical implementation and assessment of a phenomenological nonlocal model of ductile rupture. Comput. Methods Appl. Mech. Engrg. 196, 1946–1957.
Estrin, Y., 1998. Dislocation theory based constitutive modelling: foundations and applications. J. Mater. Process. Technol. 80-81, 33–39.
Estrin, Y., Toth, L.S., Molinari, A., Brechet, Y., 1998. A dislocation-based model for all hardening stages in large strain deformation. Acta Mater. 46, 5509–5522.
Ezequiel, M., Elizalde, S., Cabrera, J.M., Picas, J., Figueroa, I.A., Alfonso, I., Gonzalez, G., 2020a. Formability of the 5754-aluminum alloy deformed by a modified repetitive corrugation and straightening process. Mater. (Basel, Switzerland) 13 (633).
Ezequiel, M., Figueroa, I.A., Elizalde, S., Cabrera, J.M., Braham, C., Morin, L., Gonzalez, G., 2020b. Numerical and experimental study of a 5754-aluminum alloy processed by heterogeneous repetitive corrugation and straightening. J. Mater. Res. Technol. 9, 1941–1947.
Gensamer, M., 2017. Strength and ductility. Metall. Microstruct. Anal. 6, 171–185.
Gu, C.F., Tóth, L.S., Beausir, B., 2012. Modeling of large strain hardening during grain refinement. Scr. Mater. 66, 250–253.
Gurson, A.L., 1977. Continuum theory of ductile rupture by void nucleation and growth: Part I–Yield criteria and flow rules for porous ductile media. ASME J. Eng. Mater. Technol. 99, 2–15.
Hajizadeh, K., Ejtemaei, S., Eghbali, B., 2017. Microstructure, hardness homogeneity, and tensile properties of 1050 aluminum processed by constrained groove pressing. Appl. Phys. A 123, 504.
Huang, J., Zhu, Y.T., Alexander, D.J., Liao, X., Lowe, T.C., Asaro, R.J., 2004. Development of repetitive corrugation and straightening. Mater. Sci. Eng. A 371, 35–39.
Huang, J.Y., Zhu, Y.T., Jiang, H., Lowe, T.C., 2001. Microstructures and dislocation configurations in nanostructured Cu processed by repetitive corrugation and straightening. Acta Mater. 49, 1497–1505.
Inoue, T., Tsuji, N., 2009. Quantification of strain in accumulative roll-bonding under unlubricated condition by finite element analysis. Comput. Mater. Sci. 46, 261–266.
Jafari, M., Ziaei-Rad, S., Torabian, N., 2014. A dislocation density-based model for analyzing mechanical behavior of dual-phase steels. Metall. Microstruct. Anal. 3, 185–193.
Kawasaki, M., Horita, Z., Langdon, T.G., 2009. Microstructural evolution in high purity aluminum processed by ECAP. Mater. Sci. Eng. A 524, 143–150.
Lapovok, R., Dalla Torre, F.H., Sandlin, J., Davies, C.H.J., Pereloma, E.V., Thomson, P.F., Estrin, Y., 2005. Gradient plasticity constitutive model reflecting the ultrafine micro-structure scale: the case of severely deformed copper. J. Mech. Phys. Solids 53, 729–747.
Leblond, J.B., Kondo, D., Morin, L., Remmal, A., 2018. Classical and sequential limit analysis revisited. C. R. Méc. 346, 336–349.

Leblond, J.B., Perrin, G., Suquet, P., 1994. Exact results and approximate models for porous viscoplastic solids. Int. J. Plast. 10, 213–235.

Lu, K., 2014. Making strong nanomaterials ductile with gradients. Science 345, 1455–1456, Publisher: American Association for the Advancement of Science..

Madou, K., Leblond, J.B., 2012a. A Gurson-type criterion for porous ductile solids containing arbitrary ellipsoidal voids—I: Limit-analysis of some representative cell. J. Mech. Phys. Solids 60, 1020–1036.

Madou, K., Leblond, J.B., 2012b. A Gurson-type criterion for porous ductile solids containing arbitrary ellipsoidal voids—II: Determination of yield criterion parameters. J. Mech. Phys. Solids 60, 1037–1058.

Morin, L., Braham, C., Tajdary, P., Seddik, R., Gonzalez, G., 2021. Reconstruction of heterogeneous surface residual-stresses in metallic materials from X-ray diffraction measurements. Mech. Mater. 158, 103882.

Morin, L., Leblond, J.B., Mohr, D., Kondo, D., 2017a. Prediction of shear-dominated ductile fracture in a butterfly specimen using a model of plastic porous solids including void shape effects. Eur. J. Mech. A Solids 61, 433–442.

Morin, L., Leblond, J.B., Tvergaard, V., 2016. Application of a model of plastic porous materials including void shape effects to the prediction of ductile failure under shear-dominated loadings. J. Mech. Phys. Solids 94, 148–166.

Morin, L., Michel, J.C., Leblond, J.B., 2017b. A Gurson-type layer model for ductile porous solids with isotropic and kinematic hardening. Int. J. Solids Struct. 118, 167–178.

Mughrabi, H., 1983. Dislocation wall and cell structures and long-range internal stresses in deformed metal crystals. Acta Metall. 31, 1367–1379.

Nor, F.M., Osman, N., Kurniawan, D., 2020. Finite element analysis of repetitive corrugation and straightening die designs for severe plastic deformation of magnesium alloy. AIP Conf. Proc. 2262, 030017.

Pan, J., Saje, M., Needleman, A., 1983. Localization of deformation in rate sensitive porous plastic solids. Int. J. Fract. 21, 261–278.

Paux, J., Morin, L., Brenner, R., Kondo, D., 2015. An approximate yield criterion for porous single crystals. Eur. J. Mech. A Solids 51, 1–10.

Rahimi, F., Sadeghi, B.M., Ahmadi, M., 2018. Finite element analysis of the deformation behaviour of pure aluminium in repetitive corrugation-straightening and constrained groove pressing. Int. J. Manuf. Technol. Manage. 32, 598–609.

Reyes-Ruiz, C., Figueroa, C.G., González, G., Ortiz, A., 2021. Effect of the repetitive corrugation and straightening on the microstructure and mechanical properties of a 3003 aluminum alloy. Phys. Met. Metallogr. 122, 504–514.

Ritchie, R.O., 2011. The conflicts between strength and toughness. Nature Mater. 10, 817–822, Number: 11 Publisher: Nature Publishing Group..

Shirdel, A., Khajeh, A., Moshksar, M.M., 2010. Experimental and finite element investigation of semi-constrained groove pressing process. Mater. Des. 31, 946–950.

Tajdary, P., Morin, L., Braham, C., Gonzalez, G., 2021. A reduced single-pattern model for the numerical simulation of multi-pattern metal forming. Int. J. Mater. Form. 14, 1403–1416.

Tajdary, P., Morin, L., Romero-Resendiz, L., Gorji, M.B., Braham, C., Gonzalez, G., 2022. Analysis of shear ductile damage in forming processes using a micromechanical model with void shape effects. Int. J. Solids Struct. 248, 111640.

Tekoglu, C., Hutchinson, J.W., Pardoen, T., 2015. On localization and void coalescence as a precursor to ductile fracture. Phil. Trans. R. Soc. A 373, 20140121.

Thangapandian, N., Balasivanandha Prabu, S., Padmanabhan, K.A., 2016. Effects of die profile on grain refinement in Al–Mg alloy processed by repetitive corrugation and straightening. Mater. Sci. Eng. A 649, 229–238.

Thuillier, S., Maire, E., Brunet, M., 2012. Ductile damage in aluminium alloy thin sheets: Correlation between micro-tomography observations and mechanical modeling. Mater. Sci. Eng. A 558, 217–225.

Torkestani, A., Dashtbayazi, M.R., 2018. A new method for severe plastic deformation of the copper sheets. Mater. Sci. Eng. A 737, 236–244.

Toth, L., Molinari, A., Estrin, Y., 2001. Strain hardening at large strains as predicted by dislocation based polycrystal plasticity model. J. Eng. Mater. Technol. 124, 71–77.

Tvergaard, V., Needleman, A., 1984. Analysis of the cup-cone fracture in a round tensile bar. Acta Metall. 32, 157–169.

Valiev, R., 2004. Nanostructuring of metals by severe plastic deformation for advanced properties. Nature Mater. 3, 511–516, Number: 8 Publisher: Nature Publishing Group..

Valiev, R.Z., Estrin, Y., Horita, Z., Langdon, T.G., Zehetbauer, M.J., Zhu, Y., 2016. Producing bulk ultrafine-grained materials by severe plastic deformation: Ten years later. JOM 68, 1216–1226.

Wei, Y., Li, Y., Zhu, L., Liu, Y., Lei, X., Wang, G., Wu, Y., Mi, Z., Liu, J., Wang, H., Gao, H., 2014. Evading the strength–ductility trade-off dilemma in steel through gradient hierarchical nanotwins. Nature Commun. 5, 1–8.

Wu, X., Yang, M., Yuan, F., Wu, G., Wei, Y., Huang, X., Zhu, Y., 2015. Heterogeneous lamella structure unites ultrafine-grain strength with coarse-grain ductility. Proc. Natl. Acad. Sci. 112, 14501–14505, Publisher: Proceedings of the National Academy of Sciences..

Zenasni, Z., Haterbouch, M., Atmani, Z., Atlati, S., Zenasni, M., Nasri, K., Oussouaddi, O., 2019. Physics-based plasticity model incorporating microstructure changes for severe plastic deformation. C. R. Méc. 347, 601–614.